JOURNAL OF GEOPHYSICAL RESEARCH, VOL. 106, NO. A4, PAGES 6161–6178, APRIL 1, 2001

Modeling the quiet time inner plasma sheet protons

Chih-Ping Wang and Larry R. Lyons

Department of Atmospheric Sciences, University of California, Los Angeles, California

Margaret W. Chen

Space Science Applications Laboratory, The Aerospace Corporation, El Segundo, California

Richard A. Wolf

Department of Space Physics and Astronomy, Rice University, Houston, Texas

Abstract. In order to understand the characteristics of the quiet time inner plasma sheet protons, we use a modified version of the Magnetospheric Specification Model to simulate the bounce averaged electric and magnetic drift of isotropic plasma sheet protons in an approximately self-consistent magnetic field. Proton differential fluxes are assigned to the model boundary to mimic a mixed tail source consisting of hot plasma from the distant tail and cooler plasma from the low latitude boundary layer (LLBL). The source is local time dependent and is based on Geotail observations and the results of the finite tail width convection model. For the purpose of self-consistently simulating plasma motion and a magnetic field, the Tsyganenko 96 magnetic field model is incorporated with additional adjustable ring-current shaped current loops. We obtain equatorial proton flow and midnight and equatorial profiles of proton pressure, number density, and temperature. We find that our results agree well with observations. This indicates that the drift motion dominates the plasma transport in the quiet time inner plasma sheet. Our simulations show that cold plasma from the LLBL enhances the number density and the proton pressure in the inner plasma sheet and decreases the dawn-dusk asymmetry of the equatorial proton pressure. From our approximately force-balanced simulations the magnetic field responds to the increase of pressure gradient force in the inner plasma sheet by changing its configuration to give a stronger magnetic force. At the same time, the plasma dynamics is affected by the changing field configuration and its associated pressure gradient force becomes smaller. Our model predicts a quiet time magnetic field configuration with a local depression in the equatorial magnetic field strength at the inner edge of the plasma sheet and a cross-tail current separated from the ring current, results that are supported by observations. A scale analysis of our results shows that in the inner plasma sheet the magnitude of the Hall term in the generalized Ohm's law is not small compared with the quiet time electric field. This suggests that the frozen-in condition $\mathbf{E} = -\mathbf{v}\times\mathbf{B}$ is not valid in the inner plasma sheet and that the Hall term needs to be included to obtain an appropriate approximation of the generalized Ohm's law in that region.

1. Introduction

Plasma transport in the electric and magnetic fields of the magnetotail is crucial to understanding the plasma distributions and dynamics of the plasma sheet. Observations of the plasma sheet have revealed the large-scale structure of the plasma sheet [e.g., *Baumjohann et al.*, 1989; *Huang and Frank*, 1994] but have not been sufficiently detailed to determine the full two-dimensional distributions of plasma bulk parameters. In the central plasma sheet the observed average plasma flow is slow (~50 km/s) [*Huang and Frank*, 1986] but fast bursty flows (>400 km/s) [e.g., *Baumjohann et al.*, 1989; *Angelopoulos et al.*, 1993] are also observed.

Paper number 2000JA000377.
0148-0227/01/2000JA000377$09.00

The near–Earth portion of the plasma sheet (equatorial distances $r \sim 5$-$15\ R_E$) plays a significant role in transferring energy from the solar wind to the ionosphere through processes such as substorms, which involve strong coupling between the plasma dynamics and the electric and magnetic fields. These disturbed-time processes are initiated from a quiet time plasma sheet by an increasing convection electric field. It is thus necessary to understand the quiet time plasma sheet in order to understand the transition from quiet to disturbed conditions.

Although the mechanism behind bursty flows is not yet clear, the underlying physics of the slower drift transport is well understood. However, there has been a theoretical argument, first addressed by *Erickson and Wolf* [1980], that steady plasma transport would result in pressures in the plasma sheet that would be too high to be balanced by the magnetic forces, so that steady convection inside the magnetosphere might not be possible. However, the observations of steady magnetospheric convection events [e.g., *Yahnin et al.*, 1994]

suggest that steady convection might be possible within the plasma sheet. This disagreement reveals that the strong interaction between plasma and a magnetic field cannot be ignored [*Hau et al.*, 1989; *Sergeev et al.*, 1994] and calls for explanations from simulations.

There had been several previous efforts in modeling the plasma sheet using MHD simulations [e.g., *Ogino et al.*, 1992] or kinetic models [e.g., *Spence and Kivelson*, 1993]. Ideal MHD is a useful tool for simulating plasma and fields self-consistently. In the inner plasma sheet the energy and charge dependent magnetic drift is expected to be important and electrons and ions no longer drift together. Therefore the plasma motion is expected to violate the criteria of ideal MHD. MHD also does not allow the mixing of particles within the plasma sheet from different sources. On the other hand, the kinetic models simulate accurate drift motions in the plasma sheet but unfortunately not currently under self-consistent fields. So far, none of the simulations have provided observationally consistent plasma distributions and plasma flow in the inner plasma sheet.

In this paper, we describe and present the results of a quiet time simulation of the inner plasma sheet where an observation-based proton source is assigned to the tail boundary and proton distributions and flow in the inner plasma sheet are obtained by collecting particles drifting from their tail source under an approximately self-consistent magnetic field. The transport of plasma fluxes in our simulations is calculated from a modified version of the Magnetospheric Specification Model (MSM) [*Freeman et al.*, 1993], which simulates the bounce–averaged electric and magnetic drift of isotropic plasmas in an electric field generated from the MSM and a magnetic field generated from the Tsyganenko 96 (T96) magnetic field model [*Tsyganenko*, 1995, 1996]. The simulations are conducted under two different magnetic field configurations; one is time–independent and the other one changes approximately self-consistently with the plasma by maintaining a force balance with the plasma pressure along the midnight meridian. For the self-consistent simulation the T96 model is modified by the addition of small–scale adjustable ring-current shaped current loops. In these quiet time simulations the electric field is assumed to be very weak and time independent.

The objective of our simulation is to determine whether drift transport alone can account for the observed quiet time inner plasma sheet. The simulation also helps us to understand the contribution of the LLBL protons to the inner plasma sheet and the role of a self-consistent magnetic field in stabilizing the plasma transport.

2. Model and Simulation Description

In this section we briefly describe the assumptions and processes included in the original MSM, the electric field and magnetic field models used in our simulations, and the conditions for the quiet time simulation.

2.1. Magnetospheric Specification Model

The MSM [*Freeman et al.*, 1993] calculates the bounce–averaged electric drift and magnetic drift of a flux tube filled with an isotropic distribution of ions or electrons at a specified kinetic energy inside the closed field line region of the magnetosphere.

In slow steady flow a particle's total energy $E_K + q\Phi$ is conserved as it drifts, where E_K is the particle's kinetic energy, Φ is the electric potential, and q is the particle's electric charge. If this particle is in an isotropic particle distribution, which is a good approximation for the plasma sheet [*Stiles et al.*, 1978; *Nakamura et al.*, 1991], its bounce-averaged drift $\mathbf{v}_D$ at position $\mathbf{x}$ and time t is independent of its pitch angle and can be described as [*Wolf*, 1983]

$$\mathbf{v}_D(\mathbf{x},t)=\frac{\mathbf{B}(\mathbf{x},t)\times\nabla\Phi(\mathbf{x},t)}{|\mathbf{B}(\mathbf{x},t)|^2}+\frac{\mathbf{B}(\mathbf{x},t)\times\nabla E_k(\mathbf{x},t)}{q|\mathbf{B}(\mathbf{x},t)|^2}. \quad (1)$$

The first term on the right side of (1) is the electric drift and the second term is the magnetic drift. Particles of a given kinetic energy inside a flux tube, with no particles being added to or lost from the flux tube, drift adiabatically since individual particles conserve their total energy.

In the plasma sheet the timescale for strong pitch angle diffusion is much longer than convective timescale [*Southwood and Wolf*, 1978; *Huang et al.*, 1989]; therefore proton loss through precipitation is negligible. It has also been pointed out that waves are not strong enough to significantly change particle energies [*Huang et al.*, 1989; *Erickson*, 1992]. In addition, proton loss due to charge exchange is small in the plasma sheet. On the basis of these arguments the motion of plasma sheet particle can be regarded as adiabatic. Assuming isotropic particle distributions and adiabaticity, the kinetic energy change of drifting particles can be simply determined by the change in flux tube volume according to the relation [*Wolf*, 1983]

$$E_k=\lambda V^{-2/3},$$

where λ is constant along a particle's drift path and is called the energy invariant and V is the flux tube volume per unit magnetic flux that is defined as $V=\int ds/B$. Therefore the drift velocity (1) becomes

$$\mathbf{v}_D(\mathbf{x},t)=\frac{\mathbf{B}(\mathbf{x},t)\times\nabla(\Phi(\mathbf{x},t)+\lambda V(\mathbf{x},t)^{-2/3}/q)}{|\mathbf{B}(\mathbf{x},t)|^2}. \quad (2)$$

Using an electric and a magnetic field model to provide $\Phi(\mathbf{x}, t)$ and $V(\mathbf{x}, t)$, the drift trajectory of particles of a given energy invariant λ within a flux tube can be traced using (2).

In the model, particle flux distributions are modeled by dividing the energy spectrum into several energy channels and approximating the plasma differential flux within each energy channel by $j(E_k) = j_i(E_{ki})$, where E_{ki} is the represented kinetic energy of the ith channel. The number of ith channel particles per unit magnetic flux, η_i, can be calculated from j_i, λ_i, and V, and η_i is conserved along the drift trajectory described by (2).

The simulation starts from an initial distribution of $\eta_i(\mathbf{x}, t = 0)$ based on observed particle fluxes. At a later time t_1, particles of different λ which occupied the same flux tube at $t = 0$ have drifted apart because of their λ-dependent drift velocities (2). In the MSM, proton loss due to charge exchange is also modeled. Therefore the spatial distribution of $\eta_i(\mathbf{x})$ at $t = t_1$ is obtained by tracing the trajectories of λ_i backward in time from $t = t_1$ to $t = 0$ and reducing the η_i values at $t = 0$ by the number of particle lost by charge exchange. After getting $\eta_i(\mathbf{x}, t = t_1)$ for all energy channels, $j(\mathbf{x}, t = t_1)$ is obtained by reversing the procedure of getting η_i from j_i using $V(\mathbf{x}, t = t_1)$. The spatial distribution of plasma bulk parameters are also obtained from $\eta_i(\mathbf{x}, t = t_1)$. The plasma number density n is a summation over all energy channels within a unit flux tube volume,

$$n(\mathbf{x},\ t) = \sum_i n_i = \sum_i \frac{\eta_i(\mathbf{x},t)}{V(\mathbf{x},t)}.$$

The plasma pressure p is a summation of all partial pressure inside the flux tube,

$$p(\mathbf{x},\ t) = \sum_i p_i = \sum_i n_i(\frac{2}{3}E_{ki}) = \frac{2}{3}\sum_i \frac{\eta_i(\mathbf{x},t)}{V(\mathbf{x},t)}\lambda_i V(\mathbf{x},t)^{-2/3}$$

and the plasma temperature T is given by

$$T(\mathbf{x},\ t) = \frac{p(\mathbf{x},\ t)}{n(\mathbf{x},\ t)k_B},$$

where k_B is Boltzmann's constant.

2.2. Electric and Magnetic Field Models

The MSM calculates the bounce-averaged drift velocity (2) in the ionosphere. Therefore $\mathbf{B}(\mathbf{x}, t)$ and $\Phi(\mathbf{x}, t)$ in (2) are the Earth's dipole field and the electric field potential in the ionosphere. The electric potential in our simulation is generated by the MSM. The modeled distribution of the electric field potential at high latitudes is based on the Heppner and Maynard empirical model [*Heppner and Maynard*, 1987]. At middle and low latitudes the distribution is based on the Rice Convection Model [*Spiro et al.*, 1988], and shielding of the convection electric field is included. At auroral latitudes the electric potential is an analytic formula that gives conventional sunward convection and joins smoothly with the formula used at higher and lower latitudes. The MSM electric field model can be driven by various combinations of inputs; we assume a value for the polar cap potential drop and use *Kp* as an indicator of the size of the magnetospherically driven convection pattern.

A magnetic field model is used to calculate $V(\mathbf{x}, t)$ and map plasma distributions from the ionosphere to the equatorial plane. We use the Tsyganenko 96 (T96) magnetic field model in our simulation. One of our objectives is to understand the role of a self-consistent magnetic field in the plasma transport by investigating the difference of the inner plasma sheet resulting from quiet time transport under a constant magnetic field and under a self-consistent magnetic field. Therefore the simulation is conducted for two different magnetic field configurations. In the first simulation the magnetic field is time independent and the original T96 is used. In the second simulation the magnetic field changes consistently with plasma pressure by maintaining an approximate force balance at the equator along the midnight meridian, $(\nabla p)_x = (\mathbf{J}\times\mathbf{B})_x$. Since we only model protons, contributions from heavy ions and electrons to the plasma pressure p are neglected. The original T96 is not designed to satisfy this force balance requirement. Therefore small-scale adjustable ring-current shaped current loops [*Tsyganenko*, 1998] are added to the original T96's ring current and near-Earth cross-tail current. The current density in the current loops, $\mathbf{J}_{loop}$, changes the total current density distribution and its associated magnetic field modifies the magnetic field configuration. The force balance is maintained by adjusting $\mathbf{J}_{loop}$ so that $[(\mathbf{J}_{T96} + \mathbf{J}_{loop}) \times (\mathbf{B}_{T96} + \mathbf{B}_{loop})]_x = (\nabla p)_x$, where $\mathbf{B}_{loop}$ is the magnetic field generated by $\mathbf{J}_{loop}$ and its shielding currents on the T96's magnetopause.

2.3. Conditions for the Quiet Time Simulations

To simulate plasma sheet protons under quiet time conditions, Kp = 1 and a cross polar-cap potential drop of 26 kV are used to generate a very weak convection electric field at auroral latitudes. Contours of this convection electric field potential at the equatorial plane are shown in Figure 1. For the T96, solar wind pressure of 1 nPa, Dst = −6 nT, IMF By = 0 nT, and IMF Bz = −1 nT are used to generate a quiet magnetic field configuration.

As mentioned earlier, the simulation starts from a given spatial distribution of particle fluxes $j(\mathbf{x},\ t = 0)$ inside the model region. This initial particle flux is generated in the MSM by fitting kappa or bi-kappa distributions to *Kp*-sorted observations at L = 3, 4, 6.6, and 13 and then interpolating to every grid point inside the model region. The cold-plasma population (plasmasphere) is not included. The initial flux distribution only affects our final results for particles on closed drift trajectories. The final plasma sheet distributions depend on the imposed boundary conditions.

The particle flux $j(E_k, \mathbf{x}, t)$ at the model boundary is a source providing protons that drift into the model region. As shown in Figure 1, the model boundary (black solid curve) is located inside the plasma sheet so the particle distribution at the boundary location consists of particles that have drifted earthward in the plasma sheet after having entered from either the mantle or the low-latitude boundary layer (LLBL). The quiet time plasma sheet protons from both a distant tail and an LLBL source was first modeled by *Spence et al.* [1993]. Their results show that the plasma drifting from the distant tail is hot and tenuous in the plasma sheet while the plasma drifting from the LLBL is cold and dense. The mixture of these two populations varies with local time and is expected to be important on the dawnside of the plasma sheet. This is because protons from the duskside LLBL do not penetrate as deeply into the plasma sheet as do protons from the dawnside LLBL due to the protons' duskward drift. On the basis of this, we use a bi-kappa distribution, a sum of two kappa distributions,

$$f = N_1\left(\frac{m}{2\pi\kappa_1 E_{0,1}}\right)^{3/2}\frac{\Gamma(\kappa_1+1)}{\Gamma(\kappa_1-1/2)}\left[1+\frac{E}{\kappa_1 E_{0,1}}\right]^{-\kappa_1-1} + N_2\left(\frac{m}{2\pi\kappa_2 E_{0,2}}\right)^{3/2}\frac{\Gamma(\kappa_2+1)}{\Gamma(\kappa_2-1/2)}\left[1+\frac{E}{\kappa_2 E_{0,2}}\right]^{-\kappa_2-1}, \quad (3)$$

where N_1 and N_2 are the densities, m is particle mass, κ_1, κ_2, $E_{0,1}$, and $E_{0,2}$ are parameters of the kappa distribution (E_0 is the energy of the peak particle flux), to describe the mixing of the hot and cold populations at the dawnside model boundary. We use a single kappa distribution to describe particle fluxes at the duskside boundary. We use observations from Geotail [*Paterson et al.*, 1998] and the distribution of plasma from the LLBL source of *Spence et al.* [1993] as guidelines to construct the boundary $j(\mathbf{x}, t)$ at different local times. The locations of the tail boundary and the parameters that determine the boundary particle distributions are listed in Table 1. We have used 13 energy channels to represent proton energy spectra in our simulations. These energy channels are specified as values of λ_i that correspond to particle energies of 1 eV, 10 eV, 50 eV, 500 eV, 1 keV, 5 keV, 10 keV, 20 keV, 30 keV, 70 keV, 100 keV, 150 keV, and 200 keV at $r = 6.6\ R_E$.

In the simulations all input parameters for the MSM and T96 are kept constant. Therefore the electric field is time independent. The boundary $j(\mathbf{x}, t)$ is also kept constant to provide a steady source for protons. In the first stage of the simulation the model is run in a time-independent magnetic field until the plasma in the plasma sheet reaches a steady state, which provides a plasma sheet distribution that would

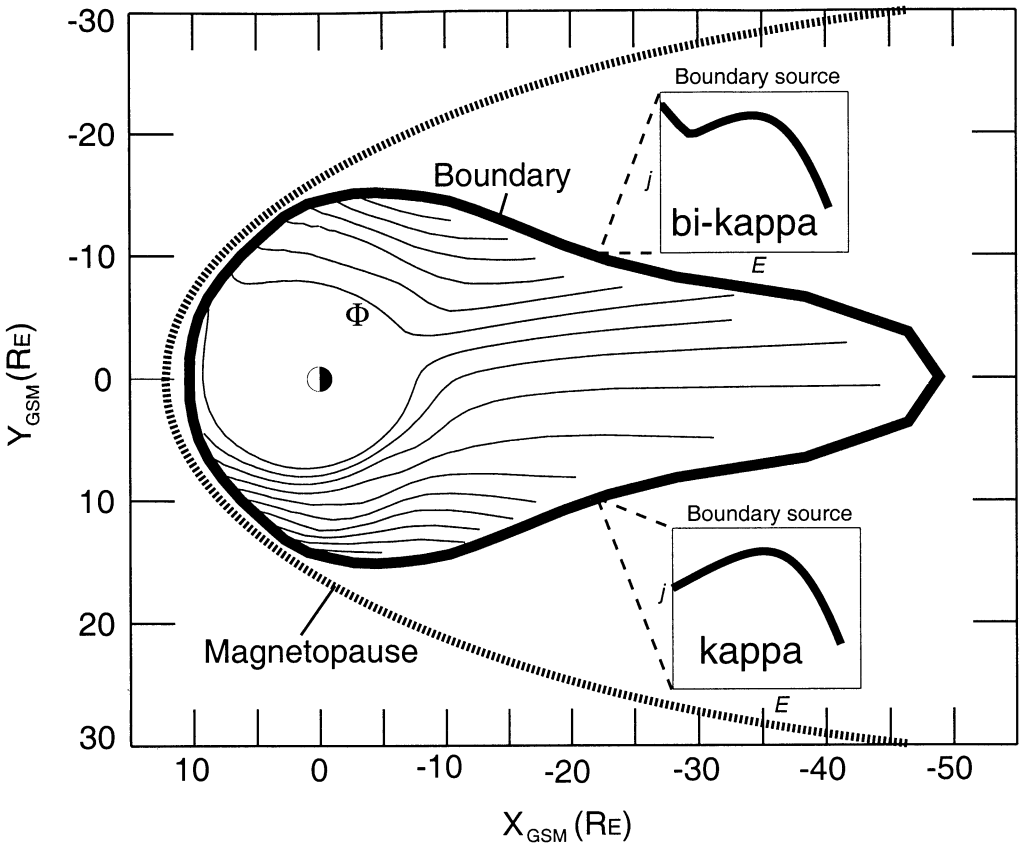

Figure 1. The model domain at the equatorial plane mapped from the ionosphere using Tsyganenko 96 model. The model boundary is indicated by thick solid line. The boundary source is assigned along and outside the model boundary. The magnetopause is indicated by thick dotted line and is determined by the Tsyganenko 96 model. Thin sold lines inside the model region are electric potential contours.

result from steady weak convection under the assumed boundary conditions and the T96 model. The second stage of the simulation starts from the steady state of the first stage and the magnetic field is adjusted so as to maintain an approximate force balance. This run continues until both the plasma and magnetic field in the plasma sheet reach a steady state, which results from the self-consistent adjustment of the magnetic field to the plasma distributions.

Table 1. The locations of the model tail boundary and the parameters that determine the boundary kappa distributions

X_{GSM}, R_E	Y_{GSM}, R_E	N_1, cm^{-3}	N_2, cm^{-3}	$E_{0,1}$, keV	$E_{0,2}$, keV	κ_1	κ_2
-12.2	-13.7	0.20	0.02	2.50	0.062	30.0	30.0
-16.6	-11.9	0.15	0.10	5.00	0.062	30.0	30.0
-19.4	-10.8	0.10	0.10	4.00	0.040	30.0	30.0
-22.9	-9.5	0.05	0.06	4.50	0.045	30.0	30.0
-28.3	-8.2	0.06	0.03	4.50	0.045	30.0	30.0
-38.3	-6.5	0.06	0.02	4.50	0.045	15.0	30.0
-46.3	-3.6	0.03	0.01	4.00	0.040	5.9	30.0
-48.8	0.0	0.03	0.01	4.00	0.040	5.9	30.0
-46.3	3.6	0.05	...	2.15	...	5.9	...
-38.3	6.5	0.12	...	1.63	...	5.9	...
-28.3	8.2	0.15	...	1.97	...	5.9	...
-22.9	9.5	0.18	...	2.23	...	30.0	...
-19.4	10.8	0.13	...	2.90	...	30.0	...
-16.6	11.9	0.24	...	3.60	...	30.0	...
-12.2	13.7	0.20	0.02	2.50	0.062	30.0	30.0

Parameters for N_2, $E_{0,2}$, and κ_2 which marked with "..." means that the distribution at that boundary location is a single-kappa distribution.

For the self-consistent simulation, although we only adjust the modification currents to maintain a force balance along the x direction, the adjustment reduces the force imbalance in the z direction as well. If the plasma and magnetic field in the plasma sheet are under a force balance, the ratios $(p(x)-\int_{x_0}^{x}(\mathbf{J}\times\mathbf{B})_x dx')/p(x=x_0)$ and $(p(z)-\int_{z_0}^{z}(\mathbf{J}\times\mathbf{B})_z dz')/p(z=z_0)$ obtained by integrating the force balance equation, $\nabla p = \mathbf{J}\times\mathbf{B}$ along the x direction and z direction, respectively should both equal 1, where x_0 and z_0 are the lower limits of integration. Figure 2a shows the ratio $(p(x)-\int_{-22R_E}^{x}(\mathbf{J}\times\mathbf{B})_x dx')/p(x=-22R_E)$ along the x direction at $z = 0$ calculated at the end of stage 1 (dashed curve) and stage 2 (solid curve) of the simulations. One can see that without self-consistent adjustments of the magnetic field (stage 1), this ratio approaches 1 for $X_{GSM} < -17$ R_E. However, with self-consistent adjustment of the magnetic field (stage 2), there is nearly force balance for -6 $R_E \geq X_{GSM} \geq -22$ R_E. Figures 2b, 2c, and 2d respectively show the ratios of $(p(z)-\int_0^z(\mathbf{J}\times\mathbf{B})_z dz')/p(z=0)$ along the z direction at $X_{GSM} = -5R_E$, $-10R_E$, and $-15R_E$. The z values where the ratios in Figures 2b-2d are truncated indicate the thickness of the plasma sheet. Figures 2b-2d show that magnetic field adjustment reduces the force imbalance in the z direction. The ratios in Figure 2 show that by incorporating adjustable current loops to the T96model at the second stage of our simulation we are able to drive plasma under an approximately force-balanced magnetic field configuration.

3. Simulation Results

In this section we discuss the results of the final steady state of the simulation, for which approximate force balance is maintained. We also compare our results with observations in the region of the plasma sheet. Evaluation of the effects of magnetic field changes required for self-consistency are discussed in section 4.

3.1. Region of the Plasma Sheet

Our simulation starts from an initial condition that includes particles on open and closed drift trajectories. After steady state is reached, particles from the initial condition remain in

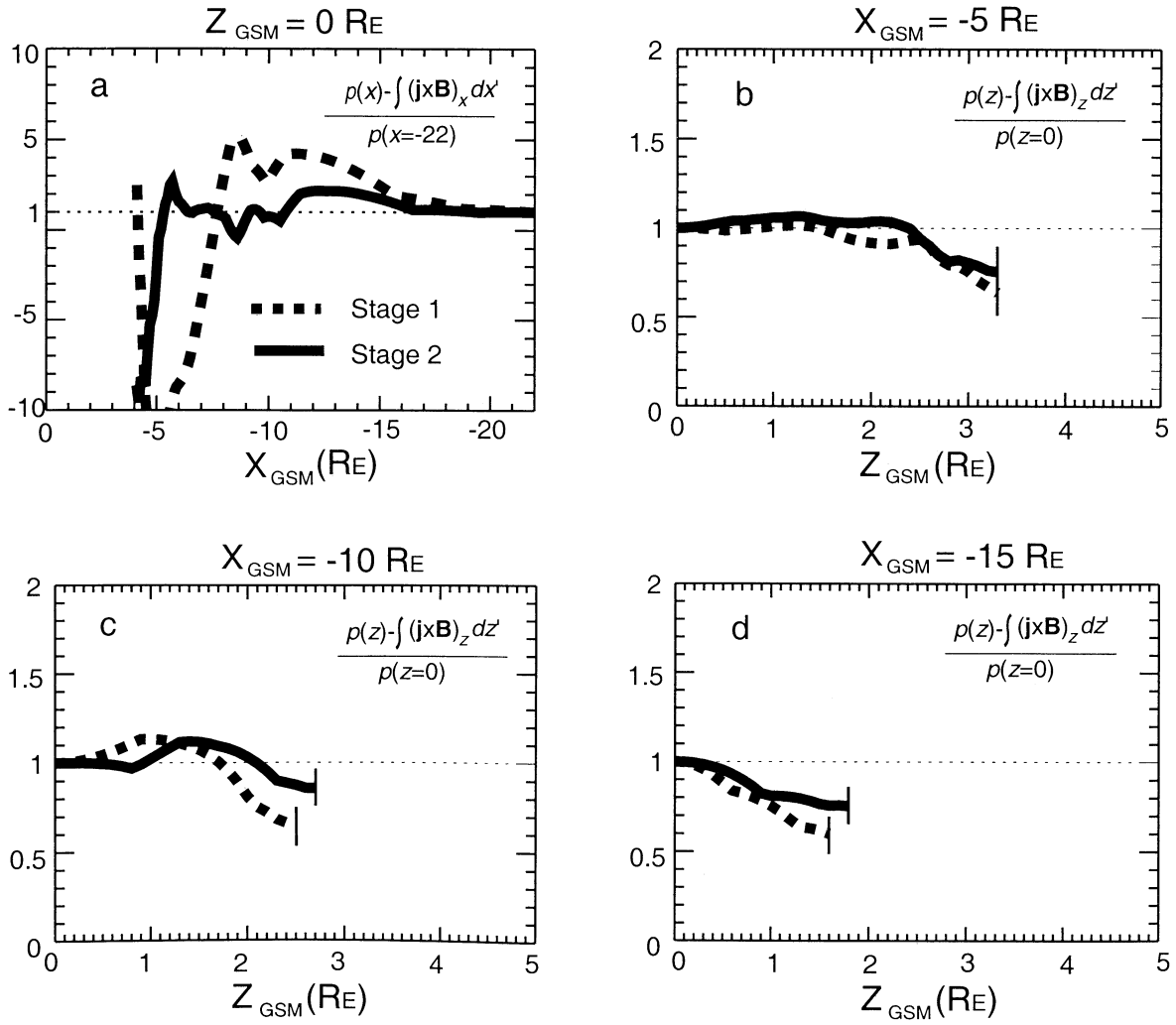

Figure 2. The ratios of $(p(x)-\int_{-22R_E}^{x}(\mathbf{J}\times\mathbf{B})_x dx')/p(x=-22R_E)$ along the x direction at the equatorial plane along the midnight meridian (a), and the ratios of $(p(z)-\int_0^z(\mathbf{J}\times\mathbf{B})_z dz')/p(z=0)$ along the z direction along the midnight meridian at $X_{GSM} = -5$ R_E (b), -10 R_E (c), and -15 R_E (d). The dashed line is from the final state of the first stage of simulations and the solid line is from the final state of the second stage. The vertical lines at the right end of lines in Figures 2b, 2c, and 2d indicate the z ranges to where the plasma sheet extends.

the magnetosphere only if they are on closed trajectories, while particles from the tail boundary source are on open trajectories. The plasma sheet, which is the focus of the current study, consists of particles drifting from the tail boundary source along open trajectories. Since our final state includes both particles on closed and open trajectories, we first distinguish contributions from particles on open and closed trajectories. Figures 3a and 3b show midnight profiles of proton pressure and number density of the initial condition (thin-dashed curve) and the final steady state (solid curve). In addition, the final steady states of pressure and density which result from particles from the boundary source only (thick-dashed curve) and from particles from the initial source only (dotted curve) are also plotted in Figure 3. As shown in Figure 3, plasma distributions beyond $X_{GSM} \sim -10\ R_E$ are determined solely by the boundary source which we have modeled to represent the real tail particle source. Between $X_{GSM} \sim -5\ R_E$ and $X_{GSM} \sim -10\ R_E$ the two sources mix. There is a transition at $X_{GSM} \sim -7\ R_E$ between particle distributions which are dominated by the tail source and those which are dominated by the initial conditions on the preexisting plasma. While the particles on closed trajectories simply represent the MSM's initial condition, and should not be regarded as a true result of our simulation, we include these particles in our final results in order to provide meaningful comparisons with observations of plasma moments from throughout the entire region where plasma sheet particles have access.

3.2. Proton Pressure

In this and following sections, we compare our simulation results to available published observations of the quiet time plasma sheet. Note that plasma parameters from different observations were obtained by averaging data over different spatial ranges around the equatorial plane or the midnight meridian and contributions from ions other than protons were included, while the simulation results are obtained by mapping

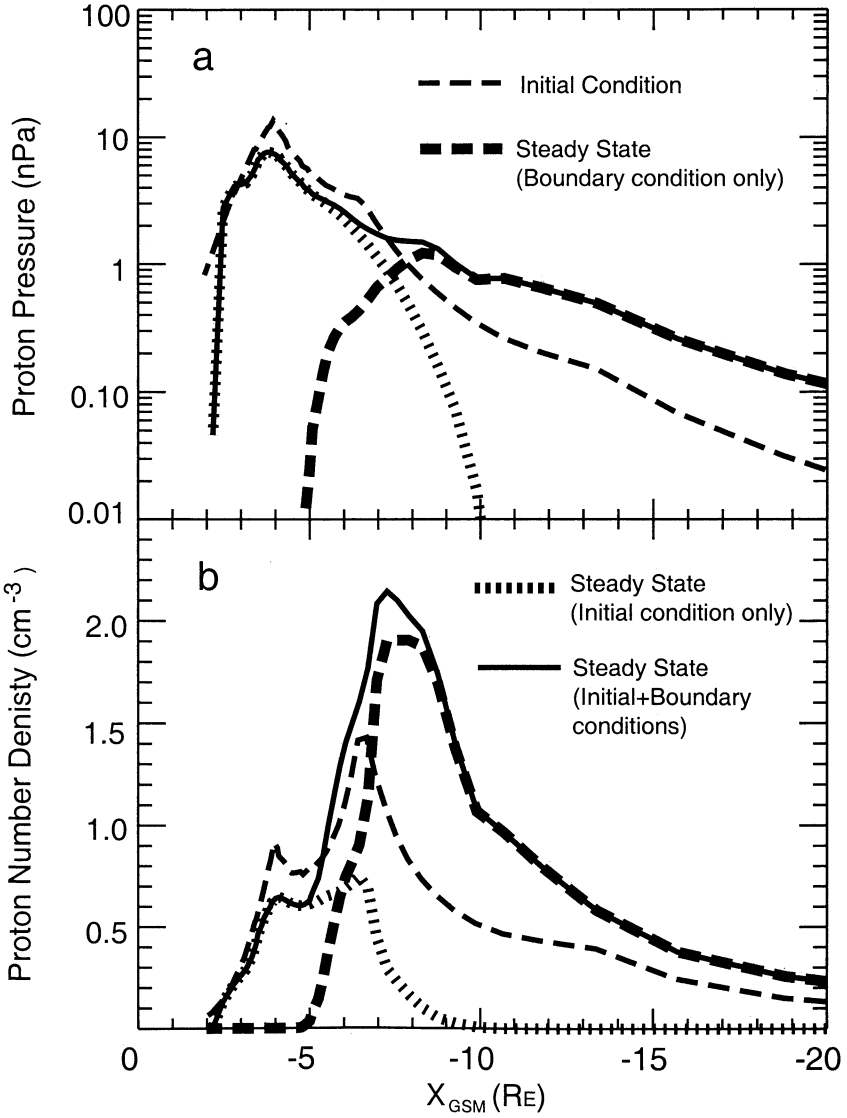

Figure 3. The proton pressure and number density along the midnight meridian determined by the initial condition (thin dashed line). Superimposed are pressure and number density at the steady state of the first stage of the simulation resulting from boundary condition only (thick dashed line), initial condition only (thick dotted line), and both boundary and initial conditions (thin solid line).

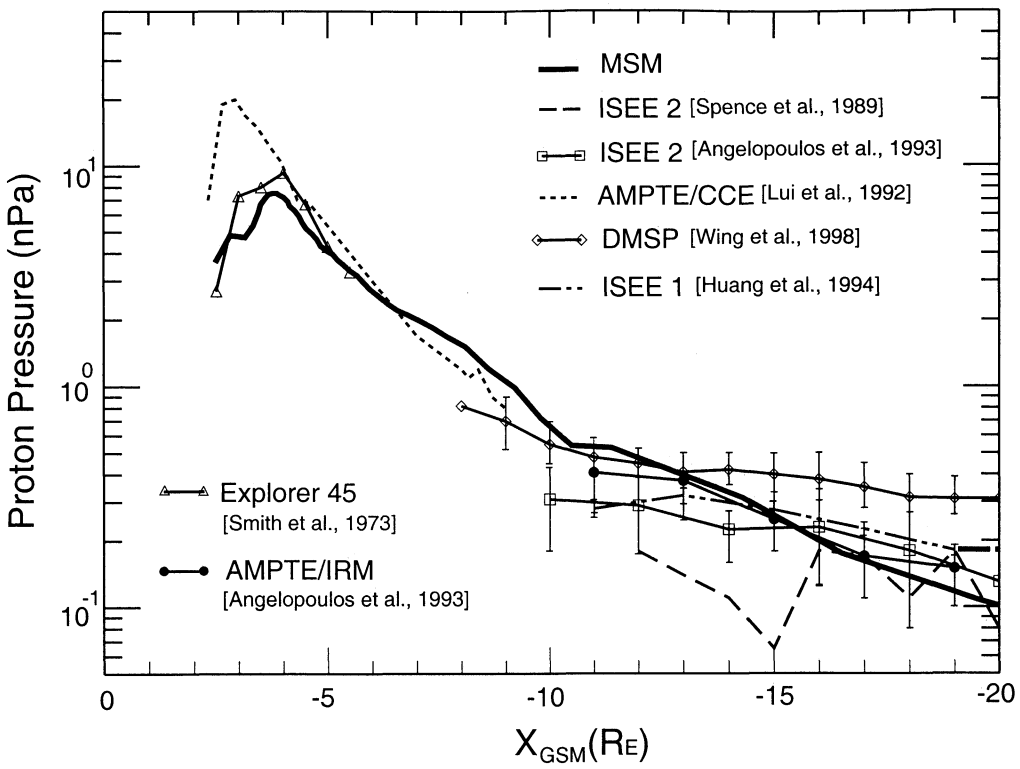

Figure 4. Quiet time steady state equatorial proton pressure (nPa) along the midnight meridian from the modified MSM (thick solid line). Superimposed are quiet time observations from DMSP (averaged values over regions $-10\ R_E < Y < 10\ R_E$), ISEE 1, ISEE 2, AMPTE/CCE, AMPTE/IRM, and Explorer 45.

simulated proton parameters from the ionosphere to the equatorial plane. Without performing the same spatial averaging as used by each observation, we focus on examining if our simulation can reproduce general distributions of the quiet time plasma sheet emerging from different observations.

The simulated total proton pressure at the equatorial plane along the midnight meridian is shown in Figure 4 and compared to observations of the quiet-time plasma sheet. In the plasma sheet, the simulated profile (thick solid curve) shows a small bump between $-10\ R_E < X_{GSM} < -7\ R_E$, a feature also seen in the observations from AMPTE/CCE [*Lui et al.*, 1992] (dotted curve shows one of their six profiles). Beyond 10 R_E, the simulated pressure decreases with increasing distance from the Earth and its magnitudes agree very well with the observations from AMPTE/IRM and ISEE2 [*Angelopoulos et al.*, 1993] (error bars show that the differences between these two sets of observations are not significant), which are averages calculated using a $2\times10\ R_E^2$ bin in the X-Y direction. Analyzing also the ISEE 2 data, *Spence et al.* [1989] obtained a pressure profile (dashed curve) different from that shown by *Angelopoulos et al.* [1993]. Their pressures, calculated by mapping data to the magnetic equator and averaging over 0.5 R_E bins in radial distance in regions $|Y_{GSM}| < 4\ R_E$, has larger fluctuations and somewhat lower values than those of *Angelopoulos et al.* [1993] between $-15\ R_E < X_{GSM} < -12\ R_E$.

The pressure profile from ISEE 1(dashed and two dots curve), which is a result of averaging data over all values of Z_{GSM} inside the plasma sheet and within $|Y_{GSM}| < 4\ R_E$ [*Huang et al.*, 1994], shows a good agreement with the AMPTE/IRM and ISEE 2 data [*Angelopoulos et al.*, 1993] throughout the plasma sheet. Although the ISEE 1 pressure is an average over data for all AE values, the data was dominated by quiet conditions. Therefore it is reasonable to include the ISEE 1 data in our comparisons. The profiles from DMSP that we use in this paper were obtained by mapping the plasma distribution from the ionosphere to the equatorial plane under the assumption of an isotropic distribution [*Wing and Newell*, 1998]. The magnitudes of the DMSP pressure averaged over $|Y_{GSM}| < 10\ R_E$ (thin solid line with hollow diamonds) are within the error bars of the AMPTE/IRM or ISEE 2 pressures [*Angelopoulos et al.*, 1993] inside $X_{GSM} > -16\ R_E$ but are higher than other observations beyond $X_{GSM} = -16\ R_E$.

Despite the range of observed pressure values in the inner plasma sheet shown in Figure 4, the main feature of increasing plasma pressure with decreasing distance from the Earth is reproduced by our simulation and the simulated pressure magnitudes are within the range of the observed pressures. With the exception of AMPTE/IRM [*Angelopoulos et al.*, 1993], the observed pressure profiles beyond 10 R_E in Figure 4 have a somewhat smaller radial pressure gradient than does the simulated pressure profile. The simulation results also compare favorably with observations at $X_{GSM} > -7\ R_E$, but it should be remembered that the simulation results in this region represent mostly the initial condition of the simulation.

Figure 5 shows the simulated pressures throughout the equatorial plane. In the plasma sheet the pressure shows a slight dawn-dusk asymmetry with higher pressure in the dusk-midnight sector. This dawn-dusk asymmetry is strongest at the inner edge of the plasma sheet and gradually becomes weaker with increasing distance from the Earth. This asymmetry results from the duskward drift motion of protons in the plasma sheet. The only observation that shows large two-dimensional coverage of the equatorial plasma pressure is the mapping of the DMSP data [*Wing and Newell*, 1998]. The DMSP pressure

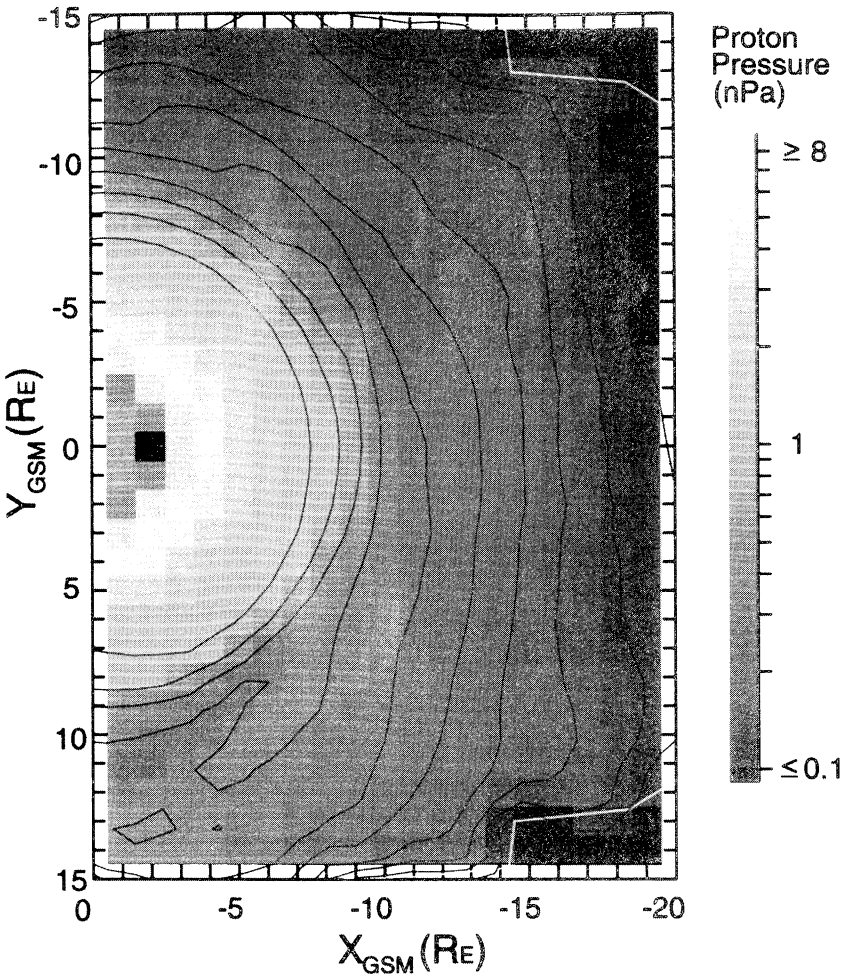

Figure 5. Quiet time steady state proton pressure (nPa) at the equatorial plane from the modified MSM.

profile shows a dawn-dusk asymmetry that we are able to reproduce successfully in our simulations (see Plate 1 of *Wing and Newell* [1998]). We next compare our simulated pressure profile along Y_{GSM} at X_{GSM} = –17 R_E with AMPTE/IRM [*Angelopoulos*, 1996] (Figure 6a) and ISEE [*Angelopoulos*, 1996] (Figure 6b) observations. The pressure, density, and temperature profiles from the AMPTE/IRM and ISEE data shown in Figure 6 are averaged over the region –16 $R_E > X >$ – 19 R_E in an aberrated GSM coordinates with a nominal 4° aberration angle [*Angelopoulos*, 1996]. The aberration is small so that direct comparisons between our results and the observations are meaningful. The pressures from ISEE ranges from 0.1 – 0.2 nPa with a slightly higher pressure on the dawnside; however, the error bar on the dawnside is also larger than on the duskside. Our result also ranges between 0.1 and 0.2 nPa but with slightly higher pressure on the duskside. The AMPTE observations do not show a dawn-dusk asymmetry; however, those measurements did not cover a wide range of Y_{AGSM}. Overall, our midnight and equatorial pressure profiles agree with most of the observations both qualitatively and quantitatively.

3.3. Proton Number Density

The simulated number density profile along the midnight meridian is shown as the thick solid curve in Figure 7. The plasma sheet density increases with decreasing distance from the Earth and reaches a peak at $X_{GSM} \approx -7$ R_E. The sharp increase of the number density at the inner edge of the plasma sheet (r = 7 -10 R_E) results from protons drifting from the dawnside boundary and is a more important factor than temperature in causing the pressure bump in this region seen in Figure 4. We compare the simulated density profile with observations from AMPTE/CCE [*Lui et al.*, 1992], ISEE 1 [*Huang et al*, 1994], and DMSP [*Wing et al.*, 1998] in Figure 7. At –6 $R_E > X_{GSM} > -9$ R_E the simulated number density is higher than the AMPTE/CCE density. However, we note that 1 keV is the lowest energy that can be detected by AMPTE/CCE so that the AMPTE/CCE data tends to underestimate the total proton density. To make a fairer comparison with the AMPTE/CCE data, we plot in Figure 7 as a dashed curve the simulated number density integrated over approximately the same energy range as AMPTE/CCE and find better agreement with the AMPTE/CCE data. Our results are almost identical to the ISEE 1 observations beyond –14 R_E and are slightly higher than the observations inside –14 R_E. In addition, a sharp density increase inside 10 R_E from our simulation agrees qualitatively with the density increase inferred from the combination of the ISEE 1 and AMPTE/CCE data. Our simulated densities are a factor 2~3 lower than the DMSP densities. *Wing and Newell* [1998] speculated that the high density from DMSP may be due to high solar wind density

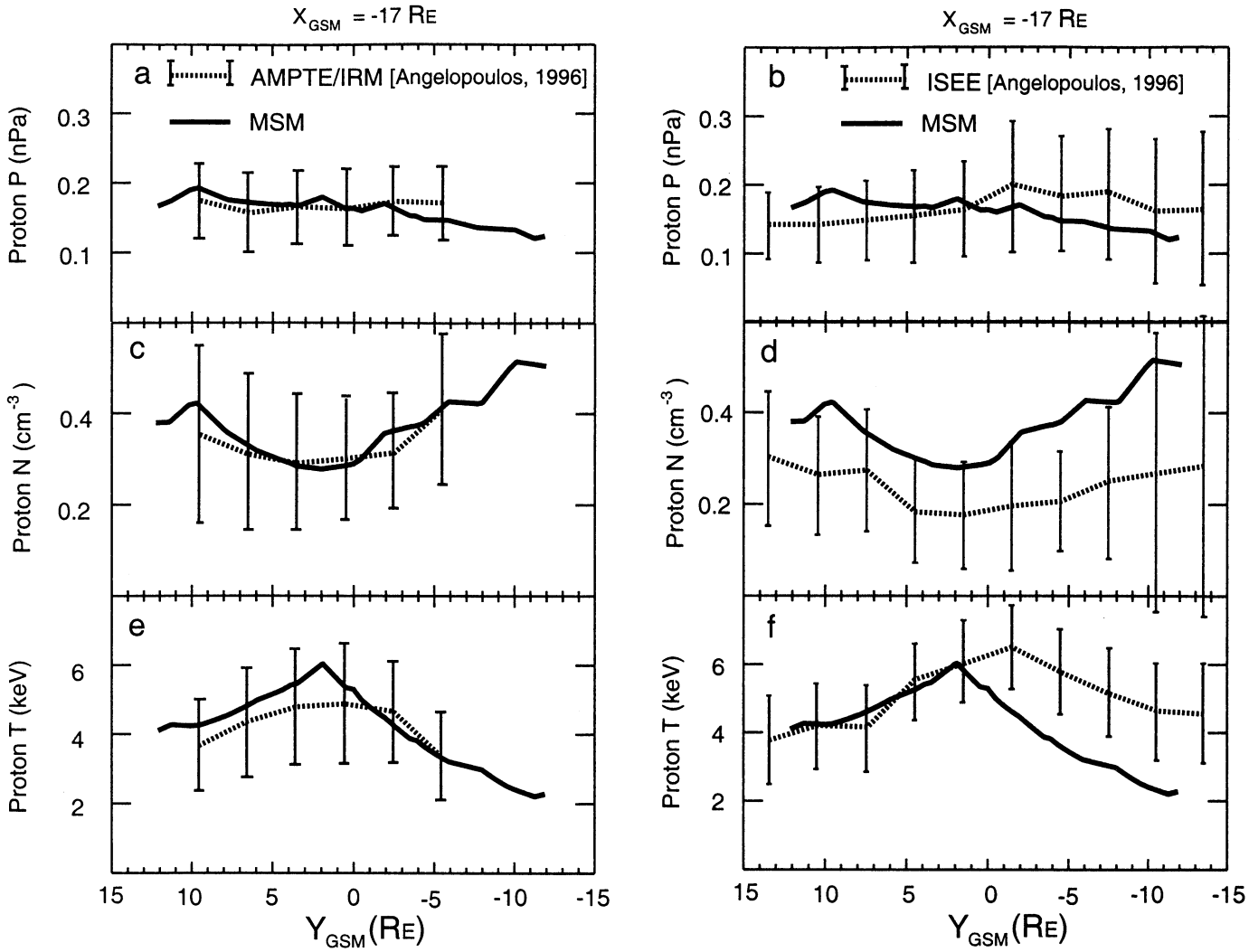

Figure 6. (a, b) Quiet time steady state proton pressure (nPa), (c, d) number density (number/cm^3), and (e, f) temperature (keV) across the tail at X_{GSM}= –17 R_E from the modified MSM (solid lines). Superimposed are quiet time observations from AMPTE/IRM (Figures 6a, 6c, and 6e) and ISEE (Figures 6b, 6d, and 6f) [*Angelopoulos*, 1996] from the region –19 R_E < X_{AGSM} < –16 R_E (dotted lines). AGSM is the aberrated GSM with a nominal 4° aberration angle.

within the time period of their data since there is a strong correlation between solar wind density and plasma sheet density [*Borovsky et al.*, 1998].

The simulated proton density in the equatorial plane is shown in Figure 8. Beyond 10 R_E, the number density is low a few R_E to the duskside of midnight and becomes higher toward dawn and dusk. This is because plasma on the dawnside and duskside of the plasma sheet consists of more cold protons which drift mainly earthward from the tail than does the plasma in midnight region. An asymmetry between the duskside and dawnside is seen with higher density on the dawnside, and this asymmetry increases with decreasing distance from the Earth. This is a result of an enhancement of cold plasma coming from the dawnside LLBL particle source. The dawn-dusk asymmetry with higher density on the dawnside is in agreement with observations reported by *Huang et al.* [1994] and *Wing and Newell* [1998] (see Plate 4 of *Wing and Newell* [1998]). Comparisons with the AMPTE/IRM and ISEE number densities [*Angelopoulos*, 1996] along Y_{GSM} are shown in Figure 6c and 6d, and it can be seen that our results agree with the observations very well, though our values are slightly higher than those observed by ISEE.

3.4. Proton Temperature

The simulated proton temperature profile along the midnight meridian is shown as the thick solid curve in Figure 9. Within the plasma sheet, the temperatures from our simulation show a slight increase with decreasing distance from the Earth. This radial variation is consistent with observations from DMSP [*Wing and Newell*, 1998], however, the ISEE 1 temperature [*Huang et al.*, 1994] appears approximately constant in this region. Our temperature, ranging from 4 to 9 keV, is close to the values from ISEE 1 but a factor of 2~3 higher than those from DMSP. In the inner magnetosphere the temperature increases rapidly to over 100 keV within the ring current region, consistent with observations from AMPTE/CCE [*Lui et al.*, 1992], though it must be remembered that this increase reflects the initial particle distributions within our model as well as our simulation of the plasma sheet.

Proton temperatures throughout the equatorial plane are shown in Figure 10. In the plasma sheet, beyond X_{GSM} ~ -15 R_E the temperature is the highest a few R_E to the duskside of midnight and decreases toward dawn and dusk. The temperature on the duskside is higher than the dawnside, consistent with the DMSP observations (Plate 3 of *Wing and Newell* [1998]). Comparison with temperatures from AMPTE/IRM and ISEE [*Angelopoulos*, 1996] along Y_{GSM} is given in Figures 6e and 6f, and it can be seen that the simulation reproduces the dawn-dusk asymmetry of the AMPTE/IRM temperatures. However, the observations from ISEE shows slightly higher temperatures than the simulated temperature on the dawnside. Inside X_{GSM} ~ −15 R_E the location of the temperature peak moves more toward the duskside with decreasing distance from the Earth within the plasma sheet. The high temperature on the duskside of the inner plasma sheet is due to the duskward motion of protons, which limits the temperature increase with decreasing distance from the Earth in the midnight profiles. The rise in temperature on the duskside of the plasma sheet increases pressure in that region. However, the equatorial pressure profile does not show as strong a dawn-dusk asymmetry as seen in the temperature profile because of the high number density on the dawnside of the plasma sheet. This will be discussed later in section 4.

3.5. Proton Flow

The average velocity $\langle \mathbf{v} \rangle$ of protons is

$$\langle \mathbf{v} \rangle = \frac{\mathbf{B} \times \nabla \Phi}{B^2} + \frac{\mathbf{B} \times \nabla p}{neB^2}, \quad (4)$$

where n is the number density and e is the electron charge. The first term on the right-hand side of (4) is the electric drift and the second term is the diamagnetic drift, which is the sum of gradient, curvature drift, and the magnetization effect.

The simulated proton flow within the equatorial plane is shown in Figure 11a and is to be compared with quiet time flows from ISEE and AMPTE/IRM [*Angelopoulos*, 1996] that are shown in Figures 11b and 11c, respectively. The magnitude of our flow is ~ 50 km/s or lower. This agrees with the observations outside L ~ 10. On the dawnside of the plasma sheet, the flow is dominated by earthward electric drift. Toward the midnight region, the duskward diamagnetic drift becomes as important as the electric drift and diverts protons toward dusk. The flow becomes earthward again toward the dusk side of the plasma sheet. The flows around the midnight are larger than the flows on two sides. Overall, the simulated two-dimensional distribution of flow directions agree well with the observations. The magnitudes also agree quite well, except inside L ~ 10 where the simulated flows speeds are consistently less than the observed flow speeds.

3.6. Quiet Time Magnetic Field and Current Density Along the Midnight Meridian

The equatorial magnetic field strength and current density along the midnight meridian is plotted in Figures 12a and 12b, respectively. The magnetic field, instead of decreasing smoothly with increasing distance from the Earth, shows a localized depression at the inner edge of the plasma sheet. This depression is also seen in the total magnetic field strength observed by AMPTE/CCE [*Lui et al.*, 1992].

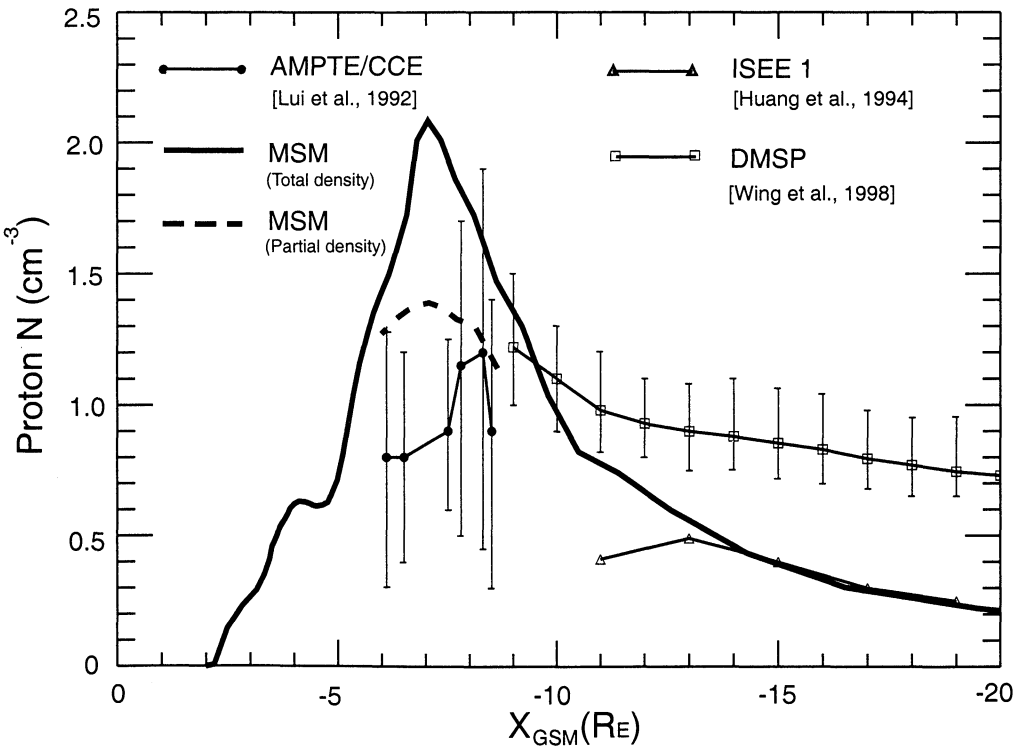

Figure 7. Quiet time steady state equatorial proton number density (number/cm^3) along the midnight meridian from the modified MSM (thick solid line). The thick dashed line between −6 R_E > X_{GSM} > −9 R_E is the partial number density obtained by integrating over λ_i for particles that have energies higher than 5 keV at r = 6.6 R_E. Superimposed are quiet time observations from DMSP (averaged values over regions −10 R_E < Y < 10 R_E), ISEE 1, and AMPTE/CCE (low-energy cutoff is 1 keV).

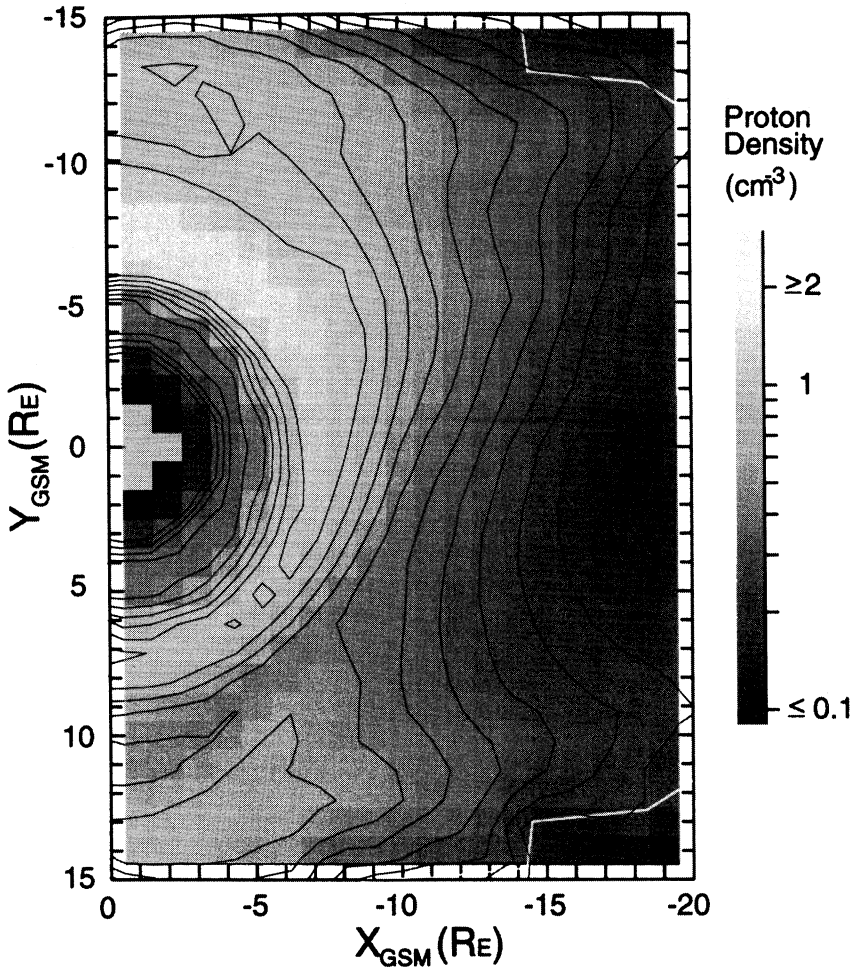

Figure 8. Quiet time steady state proton density (number/cm^3) at the equatorial plane from the modified MSM.

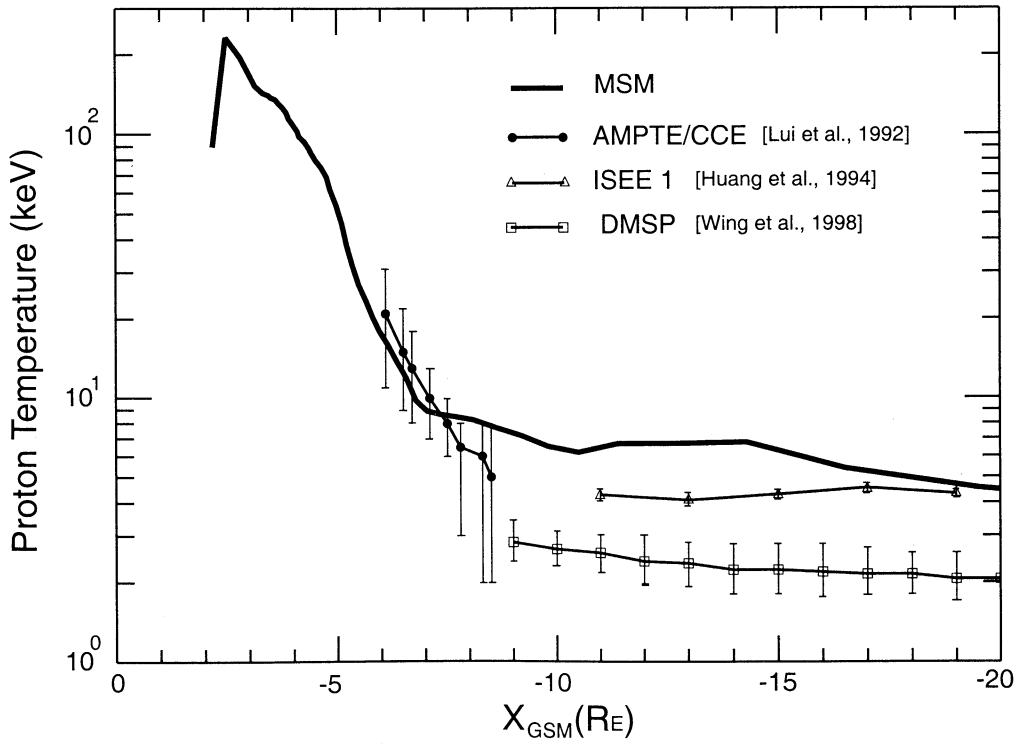

Figure 9. Quiet time steady state equatorial proton temperature (keV) in midnight meridian from the modified MSM (thick solid line). Superimposed are quiet time observations from DMSP (averaged values over regions $-10\ R_E < Y < 10\ R_E$), ISEE 1, and AMPTE/CCE.

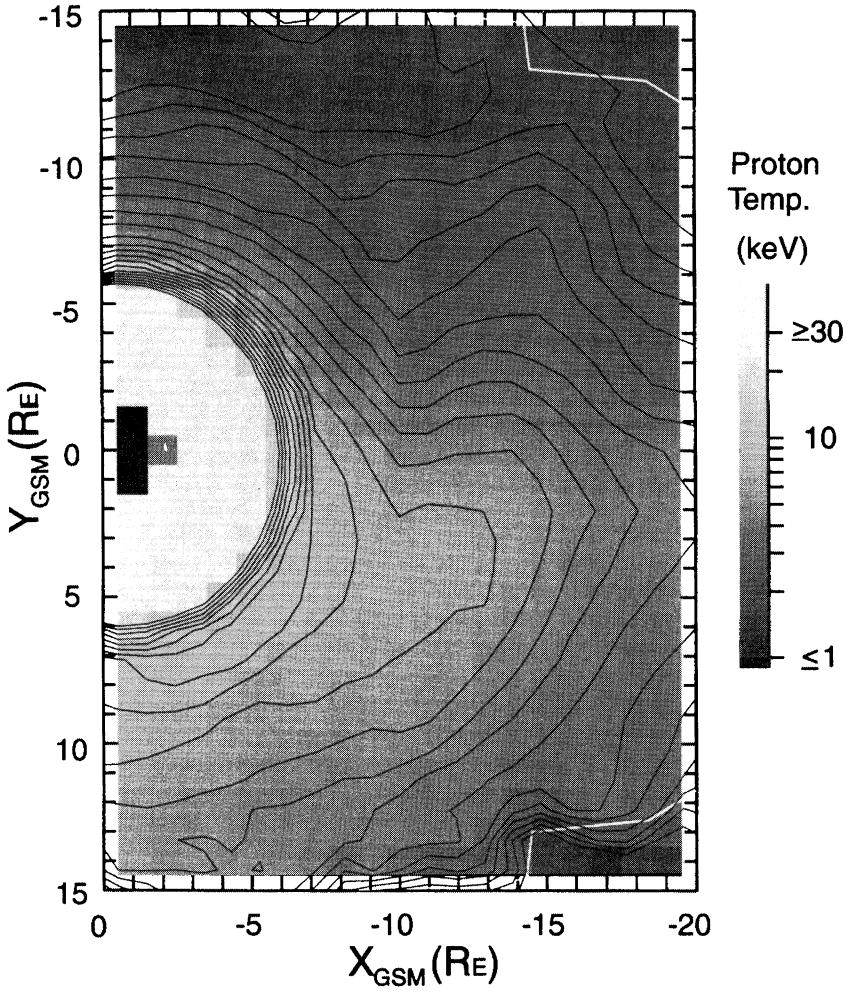

Figure 10. Quiet time steady state proton temperature (keV) within the equatorial plane from the modified MSM.

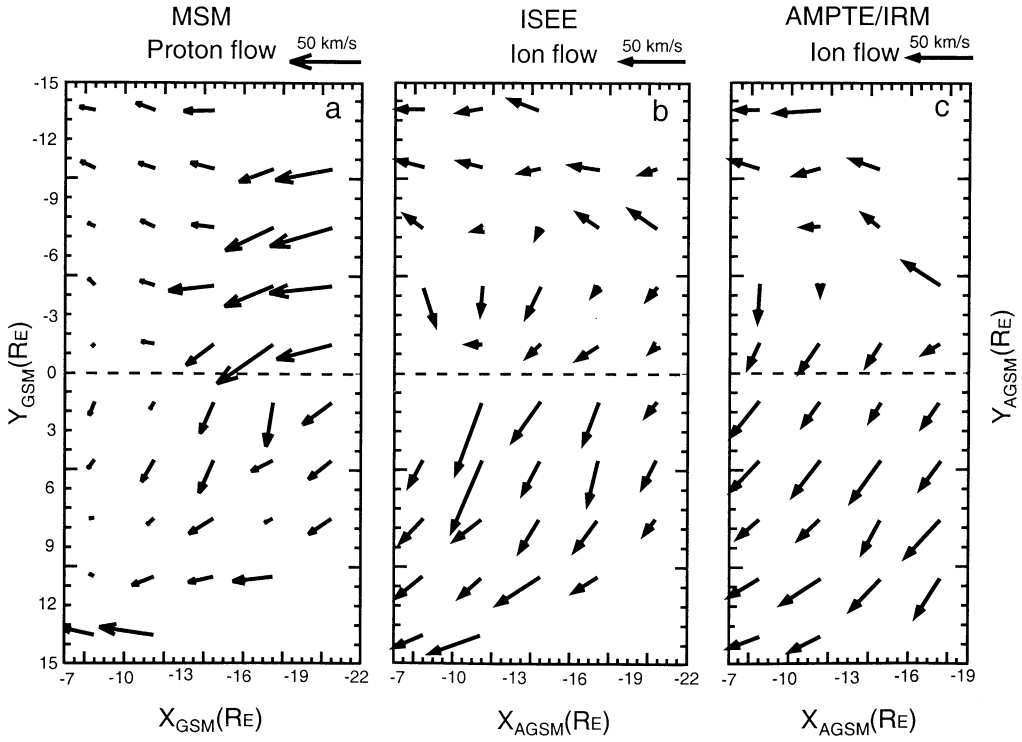

Figure 11. (a) Quiet time proton flow in the equatorial plane from the modified MSM in the GSM coordinate. The observed ion flow from (b) ISEE and (c) AMPTE/IRM [*Angelopoulos*, 1996] in the aborted GSM, AGSM, with a nominal 4° aberration angle.

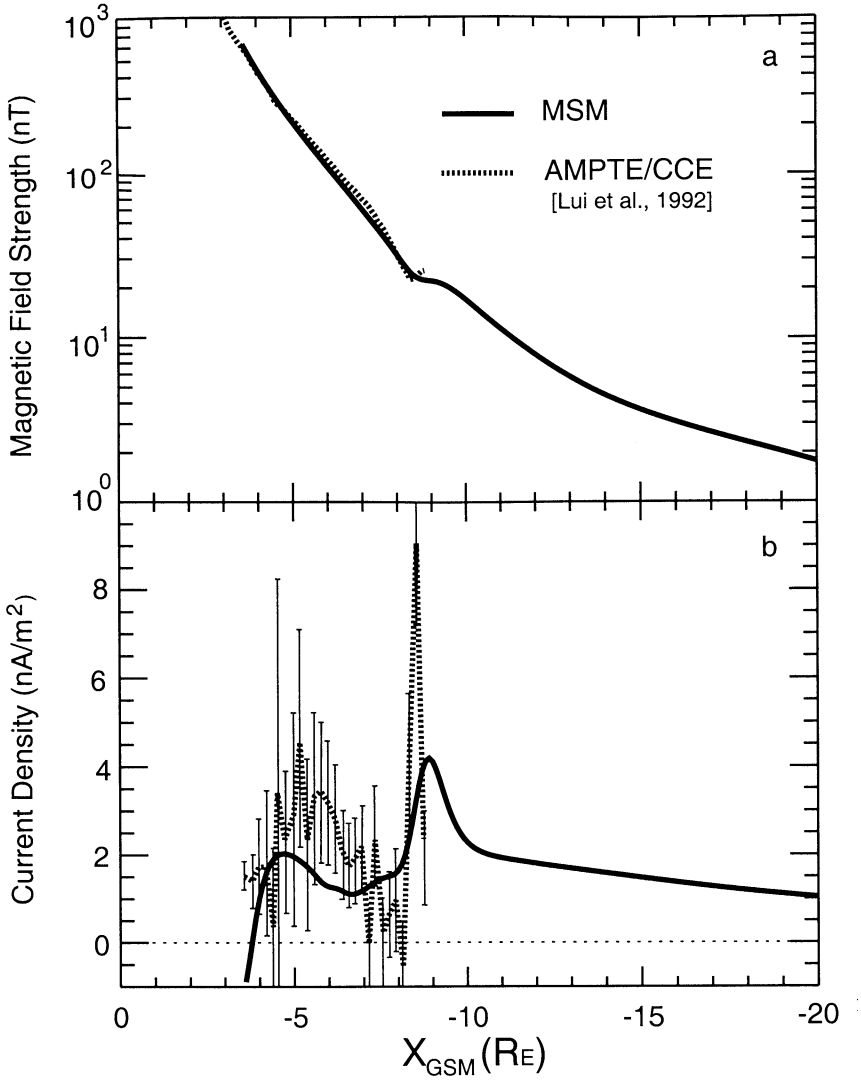

Figure 12. Equatorial (top) magnetic field strength and (bottom) current density along the midnight meridian from the modified MSM (solid lines). Superimposed are observed B_T from AMPTE/CCE and a calculated gradient current density (dotted lines) using the observed B_T and ion pressure [*Lui et al.*, 1992].

The equatorial current density, calculated from $(\nabla\times\mathbf{B}/\mu_0)_y$, shows a two-peak structure with a ring current peaked around L ~ 4 and a cross-tail current peaked at the inner edge of the inner plasma sheet. This indicates the currents in the inner magnetosphere and the plasma sheet are well separated during quiet times. This two-peak structure is confirmed by the profile of the current density, $J_\perp \approx -1/B_T(\partial p_\perp/\partial L)$, calculated by *Lui et al.* [1992] using the observed perpendicular pressure $p_\perp$ and total magnetic field B_T from AMPTE/CCE.

The features of a magnetic field depression and two-peak current structure in the force-balanced magnetic field configuration, however, are not found in the original T96 magnetic field. This difference will be discussed further in section 4.

4. Discussion

In this section we discuss how the cold protons from the LLBL contribute to the inner plasma sheet, how the interaction between a magnetic field and plasma prevents pressure inconsistency, and the importance of the Hall term in the generalized Ohm's law.

4.1. Contribution of the LLBL Source

The contribution of protons from the dawnside LLBL to the quiet time inner plasma sheet was first pointed out by *Spence and Kivelson* [1993]. Their model, which includes an LLBL source in addition to a distant tail source, predicted important features of plasma bulk parameters in the inner plasma sheet. Our equatorial pressure and temperature profiles are qualitatively consistent with their results. However, their predicted equatorial number density profile, which is relatively uniform across the tail, is different from our results. Since our distributions result from more sophisticated tail/LLBL sources and agree quantitatively with most observations, they provide more detailed information about the contribution of the LLBL source.

The mixture of plasma from the LLBL and distant tail sources in our dawnside boundary particle fluxes is described by (3), a bi-kappa distribution which consists of two single kappa distributions (see Figure 1). The high-energy portion of the dawnside boundary flux is determined by the first single kappa whose peak energy $E_{0,1}$ is chosen based on observations. Therefore there is no way to distinguish the contribution from the high-energy portion of the LLBL source

from the distant tail source for pressure-bearing protons. A second kappa distribution is added to the low-energy range of the first kappa distribution in order to model an enhancement of cold protons originating from the LLBL. Figure 13a shows the ratio of the equatorial number density obtained from a boundary source with the bi–kappa distribution (3) to those obtained form (3) without the second kappa distribution on the dawnside boundary. In Figure 13a, strong enhancements (a factor of 2 to 3) of number density are seen mainly on the dawnside of the plasma sheet because protons from the second kappa are cold and are primarily transported by an earthward electric drift. Figure 13b show the ratio of the equatorial pressure obtained form a boundary source with the bi–kappa distribution (3) to those obtained from (3) without the second kappa distribution. Including the second kappa distribution causes a 20% pressure increase on the dawnside of the inner plasma sheet. Therefore the dawn-dusk asymmetry of pressure is weaker than without considering the cold protons from the LLBL.

The existence of high number density on the dawnside plasma sheet can also be inferred from the observed earthward flow shown in Figure 11. In our simulation the number density will be a factor of 2 to 3 lower if the second kappa distribution is not included. Since the diamagnetic drift is proportional to $1/n$, the diamagnetic drift would be a factor of 2 to 3 higher without the contribution of cold protons from the LLBL. This duskward diamagnetic drift would become strong enough to distort the earthward drift so that the total drift will no longer be mainly directed earthward as observed.

4.2. Force Inconsistency

The radial pressure gradient force in the inner plasma sheet resulting from a steady earthward drift may be too strong to be balanced by the magnetic field force, which would lead to a force inconsistency that was first pointed out by *Erickson and Wolf* [1980]. Following the Erickson and Wolf paper, it was suggested that the inconsistency might be resolved by taking into account the azimuthal magnetic drift [*Tsyganenko*, 1982; *Kivelson and Spence*, 1988] and a self-consistent magnetic field [*Hau et al.*, 1989; *Erickson*, 1992]. Previous simulations have provided quantitative and self-consistent descriptions of evolving plasma and magnetic field under strong convection [e.g., *Toffoletto et al.*, 1996], though detailed comparisons with observations have not yet been presented. These models for times of strong convection indicate very weak magnetic field in the inner plasma sheet, but such weak magnetic fields are not seen in current statistics-based magnetic field models. Our simulation shows that the quiet time inner plasma sheet resulting from electric/magnetic drift can develop with an approximately self-consistent magnetic field that does not have a magnetic field minimum within the inner plasma sheet and that only differs modestly from the statistical T96 model. Our quantitative agreement with quiet time observations indicates that the force inconsistency does not exist under conditions of weak convection. Our results also support the suggestions from previous studies that the magnetic drift and self-consistent magnetic field both contribute to preventing force inconsistency. The effects of these two processes on the magnitude of the midnight plasma pressure gradient will be discussed separately in sections 4.3 and 4.4.

4.3. Effect of Magnetic Drift on Midnight Plasma Pressure

Plasma pressure p is the sum of partial pressure from particles of different energies. If magnetic drift is neglected and only electric drift drives plasma, particles of different energies within a flux tube will remain in the same flux tube as the flux tube moves and their $pV^{5/3}$ would be conserved if the

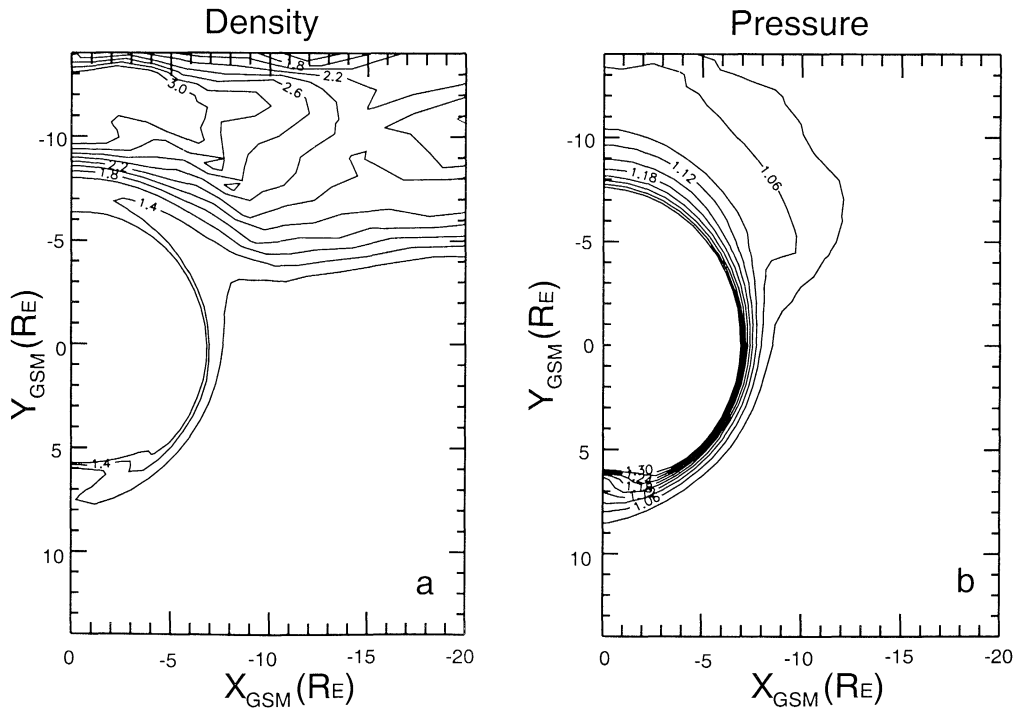

Figure 13. The ratio of (a) number density and (b) pressure resulting from a bi-kappa tail boundary source on the dawnside to those resulting from a single kappa tail boundary source on the dawn side.

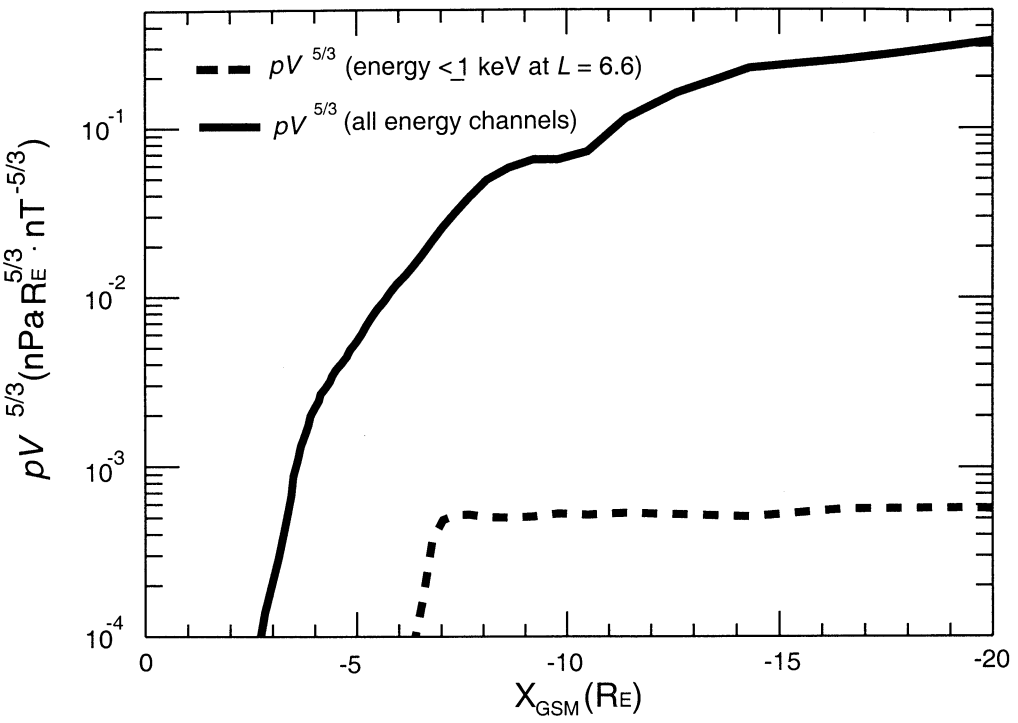

Figure 14. The $pV^{5/3}$ values along the midnight meridian. The solid line shows $pV^{5/3}$, whose p is total pressure (integrated over all energy channels) and the dashed line shows $pV^{5/3}$, whose p is integrated over λ_i for particles that have energies lower than 1 keV at $r = 6.6\ R_E$.

transport is an adiabatic process. However, when magnetic drift is involved, particles of different λ_i will not stay in the same flux tube and it is $p_iV^{5/3}$ along drift trajectories for each λ_i, not $pV^{5/3}$, which is conserved. Therefore, along the midnight meridian, the total pressure p resulting from a electric/magnetic drift would be different from the pressure resulting from electric drift alone. The difference would be small if the plasma were cold so that the electric drift dominates but will be significant in the inner plasma sheet where the plasma is hot and the magnetic drift is important.

Figure 14 shows the $pV^{5/3}$ values at the inner plasma sheet along the midnight meridian. The solid line gives the total $pV^{5/3}$, where p is the total pressure and the dashed line gives $pV^{5/3}$ where p is integrated over λ_i for particles that have energies lower than 1 keV at geosynchronous orbit. As seen in Figure 14, the $pV^{5/3}$ value for low-energy particles is almost constant in the plasma sheet, while the total $pV^{5/3}$ value decreases very rapidly with decreasing distance from the Earth. This is the consequence of the magnetic drift effect. Most of the low-energy particles remain in the same flux tube as they drift earthward from the distant tail plasma sheet so that their $pV^{5/3}$ value is almost conserved along the midnight meridian, while the high-energy particles start to leave the flux tube as their duskward magnetic drifts grow stronger with decreasing distance from the Earth. Since high-energy particles in the plasma sheet dominate low-energy particles in bearing plasma pressure, their azimuthal drift carries most of the total pressure off the midnight meridian so that the total $pV^{5/3}$ drops. Therefore the midnight pressure profile resulting from electric/magnetic drift will have a significantly lower radial pressure gradient than would result from the electric drift alone.

4.4. Effect of a Self-Consistent Magnetic Field on the Midnight Plasma Pressure

In our simulations a time-independent and plasma-independent T96 magnetic field is used during the first stage, while at the second stage the magnetic field is kept in approximate force balance with the plasma. The results, as seen in Figure 15a, shows that plasma transport under a self-consistent magnetic field would result in a slightly smaller radial pressure gradient along the midnight meridian at $L > 9$ than the transport under a rigid magnetic field. This comparison shows that when the interaction between the magnetic field and plasma brings the magnitude of the pressure gradient force down so that force inconsistency becomes less likely. As shown in Figure 15b and 15c, the force-balanced magnetic field shows specific features that result in modest but important modifications. The modifications include a modest reduction in the equatorial magnetic field strength at $L \sim 8$ and a separation of the tail and ring currents.

To physically explain the interaction that couples the magnetic field and plasma, we first describe how the plasma pressure affects the magnetic field. The rise of a cross-tail current at the inner edge of the plasma sheet shown in Figure 15c is a response to the strong pressure gradient just inside 10 R_E, which is associated with the outer side of the pressure bump that results from protons drifting from the tail source as discussed in section 3.2. The rise of a ring current in the inner magnetosphere is a response to the strong pressure gradient associated with the ring current pressure peak at 4 R_E that results from our initial condition. These two high-pressure-gradient regions are separated by a transition region at the innermost edge of the plasma sheet ($r \sim 7\ R_E$) with a relatively

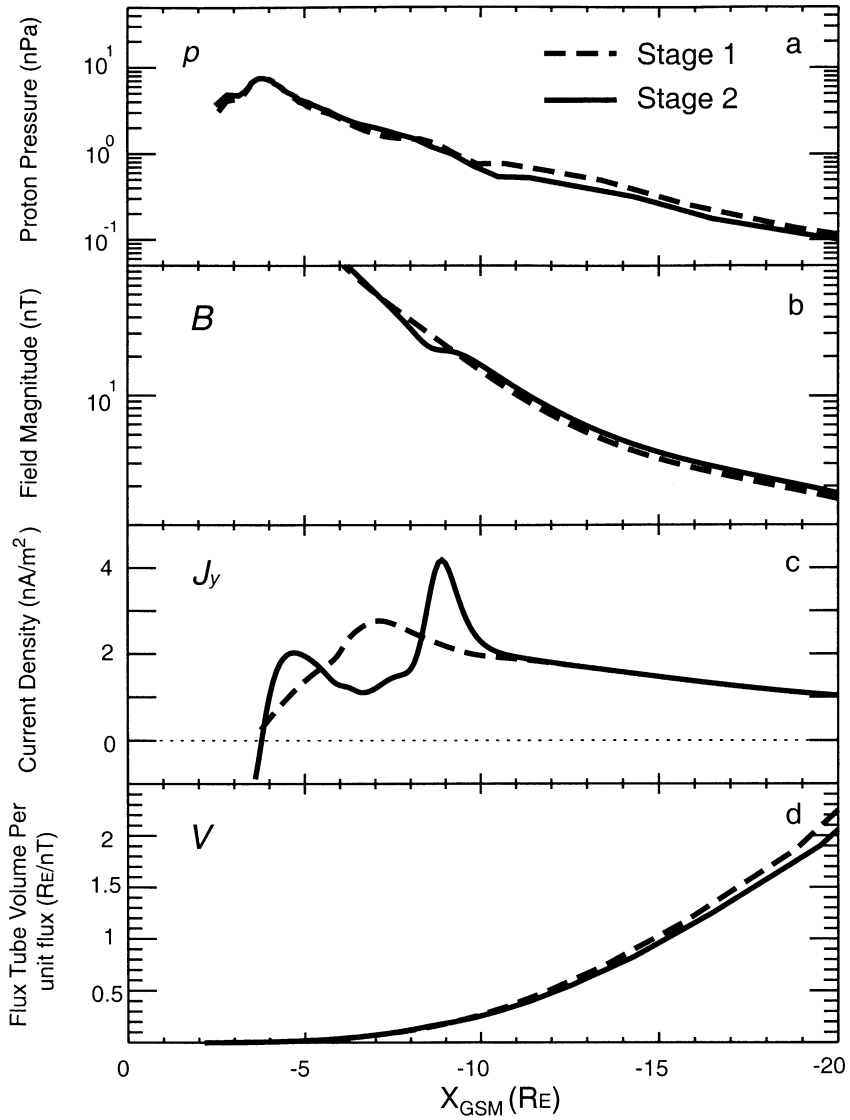

Figure 15. (a) The quiet time steady state equatorial proton pressure, (b) magnetic field strength, (c) current density, and (d) flux tube volume along the midnight meridian from the modified MSM. Solid lines are results from the simulation under a self-consistent magnetic field (stage 2) and dashed lines are results from the simulation under a time-independent magnetic field (stage 1).

small pressure gradient associated with the inner side of the pressure bump. As a consequence of balancing the small pressure gradient, the magnetic field and current density decrease in this transition region. Therefore, through the process of reaching a force balance, the magnetic field gives rise to a current density with a two-peak structure. The two separate current systems are consistent with the two well-separated populations in inner magnetosphere and plasma sheet as discussed in section 3.1. The most important feature in the force-balanced magnetic field is the formation of a modest depression on the equatorial field strength near $r = 8$ R_E. A strong field depression has been predicted by self-consistent simulations for strong convection [*Hau et al.*, 1989; *Erickson*, 1992; *Toffoletto et al.*, 1996] but is not seen in the Tsyganenko statistical magnetic field model.

The feedback from the magnetic field's reconfiguration to the plasma is that particle kinetic energies change as the flux tube volume varies. The change of flux tube volume is small in the inner magnetosphere where the field is dominated by the strong geomagnetic dipole but is significant in the plasma sheet where change of field strength has the same magnitude as the background field. As shown in Figure 15d, the flux tube volume decreases more quickly with decreasing distance from the Earth in the T96 field than in the force-balanced magnetic field. Since a particle's kinetic energy is proportional to $V^{-2/3}$, particles will gain less energy as they drift earthward under the force-balanced magnetic field than under the constant T96 field, which accounts for the smaller pressure gradient shown by the solid line in Figure 15a.

4.5. Hall Term in the Generalized Ohm's Law

The generalized Ohm's law is

$$\mathbf{E} = -\mathbf{v}\times\mathbf{B} + \frac{1}{ne}\mathbf{J}\times\mathbf{B} + \eta\mathbf{J} - \frac{1}{ne}\nabla\cdot\mathbf{p}_e + \frac{m_e}{e^2 n}\left[\frac{\partial\mathbf{J}}{\partial t} + \nabla\cdot(\mathbf{J}\mathbf{v} + \mathbf{v}\mathbf{J})\right], \quad (5)$$

where η is resistivity and $\mathbf{p}_e$ is the electron pressure tensor

[*Siscoe*, 1983]. For most space plasmas the magnitude of $-\mathbf{v}\times\mathbf{B}$ term is much larger than the other terms on the right hand side of (5) and the generalized Ohm's law can be approximated as the frozen-in condition, $\mathbf{E} = -\mathbf{v}\times\mathbf{B}$. However, the magnitude of the $\mathbf{J}\times\mathbf{B}/ne$ term, referred to as the Hall term, may become large in regions of strong current density, for example, in the region of the inner plasma sheet where the field lines are stretched. Therefore we calculate the magnitude of the Hall term at the equator along the midnight meridian using our number density profile which is shown in Figure 7, and the force-balanced magnetic field strength and current density which are shown in Figure 12. We compare the Hall term with the magnitude of the electric field used in our simulation. The comparison, shown in Figure 16, shows the Hall term is very important in the inner plasma sheet during quiet times. This scale analysis indicates that the frozen-in condition is no longer appropriate in the inner plasma sheet and that the Hall term should be included to get a better approximation of the generalized Ohm's law when modeling the inner plasma sheet.

5. Summary

We have simulated the electric and magnetic drift of protons from a mixed boundary source that represents protons originating from the distant tail and the LLBL under an approximate self-consistent magnetic field for quiet time conditions. The mixture of sources is described by a bi-kappa distribution and its local time variation is based on observations and the finite-tail-width convection model. The T96 magnetic field model is supplemented by additional adjustable ring-current shaped current loops that are adjusted self-consistently to maintain a force balance with plasma pressure along the midnight meridian at the equatorial plane.

Comparisons of the simulated plasma distributions with observations along the midnight meridian and at the equatorial plane show good agreement both qualitatively and quantitatively. The simulated drift flows reproduce well the magnitude and direction of observed flows, an important agreement with observations, which to the best of our knowledge, has not yet been shown by any other simulation. Therefore our simulation, without including bursty flows, shows that slow drift alone can account for the observed quiet time plasma sheet. This suggests that the quiet plasma sheet may be formed mainly by drift transport. The bursty flows may cause localized and temporal variations but may not be large enough to distort the large-scale drift flow and distributions.

Cold protons from the LLBL source contribute to strong enhancements of number density and weak enhancements of pressure in the dawnside plasma sheet. The increase of number of the cold protons causes total drift to be dominated by earthward electric drift on the dawnside. The increase of pressure on the dawnside helps to weaken the dawn-dusk pressure asymmetry whose higher pressure on the duskside resulting from the duskward drift of high-energy protons.

Our simulation produces an approximately force-balanced quiet time inner plasma sheet. We have investigated the effects of magnetic drift and self-consistent magnetic field on the radial pressure gradient, which have been suggested to resolve the force inconsistency initially proposed by *Erickson and Wolf* [1980]. We showed that the radial plasma pressure gradient could be reduced by these two mechanisms, which brings both plasma and magnetic field toward force balance.

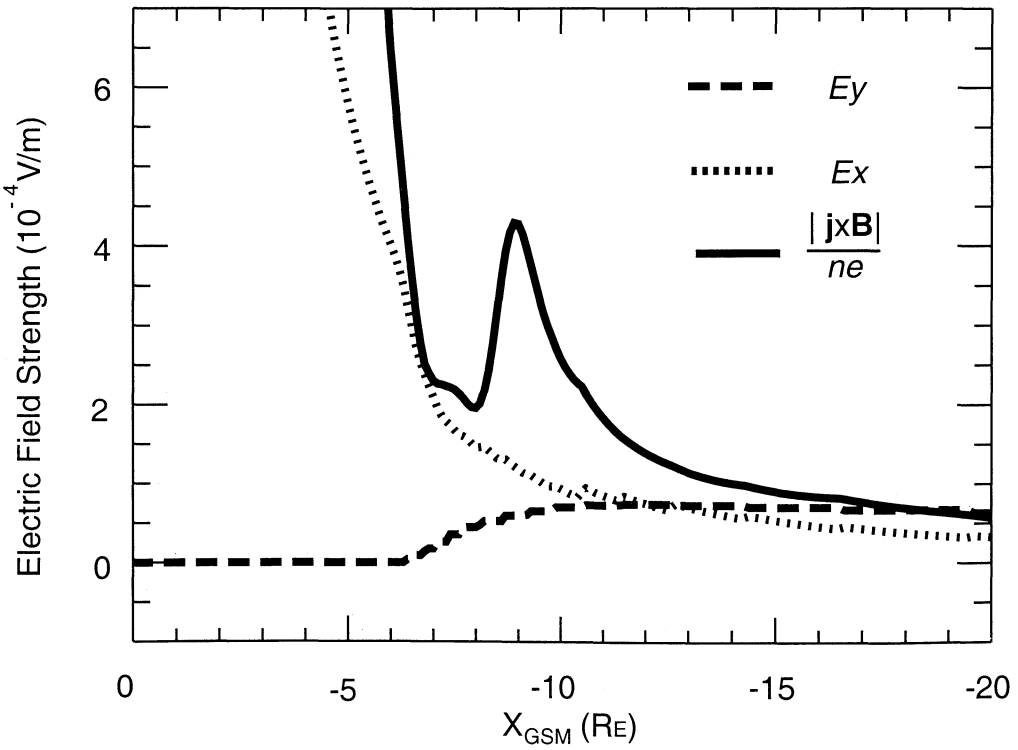

Figure 16. The magnitude of the Hall term (solid line), the x component (dotted line) and y component (dashed line) of the total electric field (corotation plus convection electric fields) at the equatorial plane along the midnight meridian from the modified MSM.

A scale analysis based on our results shows that the Hall term in the generalized Ohm's law is not small enough to be neglected in the inner plasma sheet. Therefore the frozen-in condition, $\mathbf{E} = -\mathbf{v}\times\mathbf{B}$, breaks. This suggests that $\mathbf{E} = -\mathbf{v}\times\mathbf{B} + \mathbf{J}\times\mathbf{B}/ne$ is a more appropriate approximation than the frozen-in condition for the generalized Ohm's law in the inner plasma sheet.

Encouraged by this successful attempt to simulate the quiet time inner plasma sheet, we are ready to extend our simulation to study the drift motions under an enhanced convection electric field such as happens during a substorm growth phase or a convection bay. We plan to use the results presented here as quiet time initial conditions for simulating the plasma and magnetic field changes which occur after the convection electric field is enhanced.

Acknowledgments. We should like to thank N. A. Tsyganenko for his assistance in making modifications to the Tsyganenko 96 magnetic field model. This work has been supported at UCLA by NSF grant ATM-981698. The work by M. W. Chen has been supported by NSF grants NSF-ATM-9522288 and NSF-ATM-9900981and the Aerospace Technical Investment Program. The work by R. A. Wolf has been supported by NASA grant NAG5-8136.

Janet G. Luhmann thanks Haje Korth and another referee for their assistance in evaluating this paper.

References

Angelopoulos, V., et al., Characteristics of ion flow in the quiet state of the inner plasma sheet, *Geophys. Res. Lett., 20*, 1711–1714, 1993.

Angelopoulos, V., The role of impulsive particle acceleration in magnetotail circulation, in *Proceedings of the Third International Conference on Substorms (ICS-3), Eur. Space Agency Spec. Publ., ESA SP-389*, 17–22, 1996.

Baumjohann, W., G. Paschmann, and G. A. Cattell, Average plasma properties in the central plasma sheet, *J. Geophys. Res., 94*, 6597–6606, 1989.

Borovsky, J. E., M. F. Thomsen, and R. C. Elphic, The driving of the plasma sheet by the solar wind, *J. Geophys. Res., 103*, 17,617–17,639, 1998.

Erickson, G. M., A quasi-static magnetospheric convection model in two dimensions, *J. Geophys. Res., 97*, 6505–6522, 1992.

Erickson, G. M., and R. A. Wolf, Is steady convection possible in the Earth's magnetotail, *Geophys. Res. Lett., 7*, 897–900, 1980.

Freeman, J. W., R. A. Wolf, R. W. Spiro, and B. Hausman, B. Bales, R. Hilmer, A. Nagai, and R. Lambour, Magnetospheric specification model development code documentation, scientific description, and software documentation, contract F19628-90-K-0012, Rice Univ. for Air Force Geophy. Lab., Hanscom Air Force Base, Mass., July 1993.

Hau, L.-N., R. A. Wolf, G.-H. Voigt, and C. C. Wu, Steady state magnetic field configurations for the Earth's magnetotail, *J. Geophys. Res., 94*, 1303–1316, 1989.

Heppner, J. P., and N. C. Maynard, Empirical high-latitude electric field models, *J. Geophys. Res., 92*, 4467, 1987.

Huang, C. Y., and L. A. Frank, A statistical survey of the central plasma sheet: implications for substorm models, *Geophys. Res. Lett., 13*, 652-655, 1986.

Huang, C. Y., and L. A. Frank, A statistical survey of the central plasma sheet, *J. Geophys. Res., 99*, 83–95, 1994.

Huang, C. Y., C. K. Goertz., and L. A. Frank, Observational determination of the adiabatic index in the quiet time plasma sheet, *Geophys. Res. Lett., 16*, 563-566, 1989.

Kivelson, M. G., and H. E. Spence, On the possibility of quasi-static convection in the quiet magnetotail, *Geophys. Res. Lett., 15*, 1541–1544, 1988.

Lui, A. T. Y., and D. C. Hamilton, Radial profiles of quiet time magnetospheric parameters, *J. Geophys. Res., 97*, 19,325–19,332, 1992.

Nakamura, M., G. Paschmann, W. Baumjohann, and N. Sckopke, Ions distributions and flows near the neutral sheet, *J. Geophys. Res., 96*, 5631–5649, 1991.

Ogino, T., R. J. Walker, and M. Ashour-Abdalla, A global magnetohydrodynamic simulation of the magnetosheath and magnetosphere when the interplanetary magnetic field is northward, *IEEE Trans. Plasma Sci., 20*, 817–828, 1992.

Paterson, W. R., L. A. Frank, S. Kokubun, and T. Yamamoto, Geotail survey of ion flow in the plasma sheet: Observations between 10 and 50 R_E, *J. Geophys. Res., 193*, 11,811–11,825, 1998.

Sergeev, V. A., T. I. Pulkkinen, R. J. Pellinen, and N. A. Tsyganenko, Hybrid state of the tail magnetic configuration during steady convection events, *J. Geophys. Res., 99*, 23,571–23,582, 1994.

Siscoe, G. L., Solar system magnetohydrodynamics, in *Solar-Terrestrial Physics*, edited by R. L. Carovillano and J. M. Forbes, p. 11, D. Reidel, Norwell, Mass., 1983.

Southwood, D. J., and R. A. Wolf, An assessment of the role of precipitation in magnetospheric covection, *J. Geophys. Res., 83*, 5227-5232, 1978.

Spence, H. E., and M. G. Kivelson, Contributions of the low–latitude boundary layer to the finite width magnetotail convection model, *J. Geophys. Res., 98*, 15,487–15,496, 1993.

Spence, H. E., M. G. Kivelson, R. J. Walker, and D. J. McComas, Magnetospheric plasma pressures in the midnight meridian: observations from 2.5 to 35 R_E, *J. Geophys. Res., 94*, 5264–5272, 1989.

Spiro, R. W., R. A. Wolf, and B. G. Fejer, Penetration of high-latitude-electric-field effects to low latitudes during SUNDIAL 1984, *Ann. Geophys., 6*, 39–50, 1988.

Stiles, G. S., E. W. Hones Jr., S. J. Bame, and J. R. Asbridge, Plasma sheet pressure anisotropies, *J. Geophys. Res., 83*, 3166–3172, 1978.

Toffoletto, F. R., R. W. Spiro, R. A. Wolf, M. Hesse, and J. Birn, Self-consistent modeling of inner magnetospheric convection, in *Proceedings of Third International Conference on Substorms (ICS-3), Eur. Space Agency Spec. Publ.*, edited by E. J. Rolfe and B. Kaldeich, *ESA SP-389*, 223–230, 1996.

Tsyganenko, N. A., On the convective mechanism for formation of the plasma sheet in the magnetospheric tail, *Planet. Space Sci., 30*, 1007–1012, 1982.

Tsyganenko, N. A., Modeling the Earth's magnetospheric magnetic field confined within a realistic magnetopause, *J. Geophys. Res., 100*, 5599–5612, 1995.

Tsyganenko, N. A., Effects of the solar wind conditions on the global magnetospheric configuration as deduced from data-based field models, in *Proceedings of the ICS-3 Conference on Substorms, Eur. Space Agency Spec. Publ., ESA SP-389*, 181–185, 1996.

Tsyganenko, N. A., Data-based models of the global geospace magnetic field: challenges and prospects of the ISTP Era, in *Geospace Mass and Energy Flow: Results From the International Solar-Terrestrial Physics Program*, edited by J. L. Horwitz, D. L. Gallagher, and W. K. Peterson, pp. 371–382, AGU, Washington, D. C., 1998.

Wing, S., and P. T. Newell, Central plasma sheet ion properties as inferred from ionospheric observations, *J. Geophys. Res., 103*, 6785–6800, 1998.

Wolf, R. A., The quasi–static (slow–flow) region of the magnetosphere, in *Solar Terrestrial Physics*, edited by R. L. Carovillano and J. M. Forbes, pp. 303–368, D. Reidel, Norwell, Mass., 1983.

Yahnin, A. G., et al., Features of steady magnetospheric convection, *J. Geophys. Res., 99*, 4039–4051, 1994.

M. W. Chen, Space Science Applications Laboratory, The Aerospace Corporation, P.O. Box 92957 M2-260, Los Angeles, CA 90009. (Margaret.W.Chen@aero.org)

L. R. Lyons and C.-P. Wang, Department of Atmospheric Sciences, University of California, Los Angeles, 405 Hilgard Avenue, Los Angeles, CA 90095. (larry@atmos.ucla.edu; cat@atmos.ucla.edu)

R. A. Wolf, Department of Space Physics and Astronomy, Rice University, Houston, TX 77251. (wolf@alfven.rice.edu)

(Received September 29, 2000; revised November 13, 2000; accepted November 14, 2000.)